




# Two-stage warm cross rolling and its effect on the microstructure, texture and magnetic properties of an Fe-6.5 wt% Si non-oriented electrical steel

Haijie Xu<sup>1,2,3</sup>, Yunbo Xu<sup>1,\*</sup> , Youliang He<sup>2,\*</sup>, Sifei Cheng<sup>1</sup>, Haitao Jiao<sup>1</sup>, Steve Yue<sup>3</sup>, and Jianping Li<sup>1</sup>

<sup>1</sup> State Key Laboratory of Rolling Technology and Automation, Northeastern University, Shenyang 110819, P. R. China

<sup>2</sup> CanmetMATERIALS, Natural Resources Canada, Hamilton, ON L8P 0A5, Canada

<sup>3</sup> Department of Materials Engineering, McGill University, Montreal, QC H3A 2B2, Canada

Received: 26 December 2019

Accepted: 20 May 2020

Published online:

3 June 2020

© Crown 2020

## ABSTRACT

Cross rolling is an effective processing technique used to optimize the crystallographic texture of electrical steel sheets. However, it is usually applied in *cold rolling* only. It is unknown how this rolling technique affects the microstructure and texture of electrical steels at elevated temperatures. In this study, a two-stage *warm cross rolling* scheme, i.e., rolling at elevated temperatures and in alternative directions with respect to the hot rolling direction (HRD), was applied to an Fe-6.5 wt% Si non-oriented electrical steel to produce thin steel sheets. The swapping of rolling direction between the two warm rolling stages significantly changed the deformation microstructure and texture, leading to different final recrystallization textures. These differences are attributed to the discrepancies in slip activities at elevated temperatures and to the different initial textures resulted from the change in rolling direction. The magnetic properties of the final steel sheets are evaluated by single sheet testing. Although the steel processed by warm rolling along HRD in the first stage and along HTD in the second stage exhibits a slightly higher magnetic flux density than other routes, it is shown that the magnetic flux density and core loss may have little relation to the crystallographic texture since the magnetocrystalline anisotropy caused by the texture is small.

## Introduction

Electrical steels with silicon content up to ~ 3.5 wt% have been a widely used soft magnetic material for many applications, including transformers and rotating machines [1–4]. When the silicon content is

further increased to ~ 6.5 wt%, the steel shows superior magnetic properties, e.g., low core losses and near-zero magnetostriction [5–8], thus having great potential to reduce energy loss and decrease noise. However, due to the formation of ordered phases in this steel, the formability at room

Address correspondence to E-mail: yunbo\_xu@126.com; youliang.he@canada.ca

temperature is extremely low, and it is essentially not possible to directly cold roll this steel to produce thin sheets. Thus, a warm rolling process is normally needed to improve the formability so that final cold rolling can be applied.

For non-oriented electrical steels used in electric motors, it is desired that a  $\langle 001 \rangle // \text{ND}$  (normal direction) texture be produced in the steel sheets after rolling and annealing, since this texture aligns the crystals' easy  $\langle 100 \rangle$  axes to the magnetization directions, leading to good magnetic properties [1, 9–11]. However, it is very difficult to produce this texture in high silicon steels through conventional rolling and annealing, since  $\langle 111 \rangle // \text{ND}$  ( $\gamma$ -fiber) and  $\langle 110 \rangle // \text{RD}$  (rolling direction,  $\alpha$ -fiber) are usually the final textures after conventional rolling and annealing [12, 13]. Thus, alternative rolling schemes have been developed to optimize the final textures of electrical steels, and the most widely studied technique was cross rolling.

Vanderschueren [14] and Kestens [12] used cross rolling to produce a strong  $\langle 100 \rangle // \text{ND}$  texture in electrical steels and pointed out that an  $\alpha$ -fiber texture was transformed to an unstable  $\langle 110 \rangle // \text{TD}$  (transverse direction) texture by rotating the hot band around the ND by  $90^\circ$  before cold rolling. This texture ( $\langle 110 \rangle // \text{TD}$ ) was then transformed into the stable  $\{001\} \langle 110 \rangle$  (rotated cube) texture during cold rolling, resulting in a strong  $\langle 100 \rangle // \text{ND}$  texture after annealing. Yan and Fu [15] attributed the formation of the  $\{001\} \langle 110 \rangle$  rolling texture in 3.0 wt% Si steel to hindered dislocation movement and accelerated rotation of the  $\{112\} \langle 111 \rangle$  grains. Ushigami et al. [16] reported a three-pass cross rolling technique, in which the rolling direction of the second pass was perpendicular to those of the first and third passes, which led to the formation of the Goss ( $\{011\} \langle 100 \rangle$ ) and cube ( $\{001\} \langle 100 \rangle$ ) textures after annealing. Sonboli et al. [17] investigated a two-stage cross rolling process with intermediate annealing, in which the first stage was carried out in the hot rolling direction (HRD), i.e., conventional rolling, while the second stage was in the hot transverse direction (HTD). After final annealing, a strong  $\{001\} \langle 100 \rangle$  texture was developed.

The above-mentioned studies demonstrated that cross rolling was indeed able to optimize the final annealing texture in electrical steels. However, all these studies were conducted at room temperature and were focused on electrical steels with Si contents

less than  $\sim 3.5$  wt%. Very few investigations have been carried out on steels containing 4.5 wt% or more silicon. For electrical steels with silicon up to  $\sim 3.5$  wt%, cross rolling can be readily applied at room temperature because of the good formability of these steels. For the 6.5 wt% Si steel, the extremely poor room-temperature workability prohibits the direct application of cold rolling on the hot band. Thus, a warm rolling process is generally required before cold rolling. On the other hand, warm rolling may be directly employed as a final rolling process to produce thin steel sheets. Thus, it is of interest to investigate how warm cross rolling affects the evolution of microstructure and texture during the processing of high silicon steels.

## Material and experimental procedure

The investigated electrical steel contained (wt%): 6.5 Si, 0.009 C, 0.011 Mn, 0.005 Al, 0.005 S and 0.0002 N. The alloy was melted in a vacuum induction furnace and cast into a  $\Phi 100$  mm  $\times$  180 mm (diameter  $\times$  height) ingot. The ingot was homogenized at  $1200^\circ\text{C}$  for 2 h and forged into a billet with a thickness of 70 mm. The billet was reheated to  $1200^\circ\text{C}$  (held for 30 min) and hot rolled to a thickness of 2.0 mm in a reversing rolling mill (with  $\sim 97\%$  thickness reduction). After hot rolling, four rectangular plates of 75 mm (width)  $\times$  85 mm (length) were cut from the hot-rolled plate. These plates were distinguished according to the way they were cut from the hot plate: those with the longitudinal direction (85 mm) parallel to the hot rolling direction (HRD) were designated as A and B, while those with the longitudinal direction parallel to the hot transverse direction (HTD) were designated as C and D. The detailed processing scheme is shown in Fig. 1.

During the two-stage warm rolling process, the rolling directions of the four plates were altered from the HRD to HTD, or vice versa, resulting in a total of 4 different combinations (first stage-second stage): HRD-HRD, HRD-HTD, HTD-HTD, and HTD-HRD, corresponding to Routes A, B, C, and D, respectively (Fig. 1). The first stage warm rolling was carried out at  $650^\circ\text{C}$ , with a 40% thickness reduction (from 2.0 mm to 1.2 mm). The second stage was conducted at  $450^\circ\text{C}$ , with a thickness reduction of 58% (from 1.2 mm to 0.5 mm). Apparently, Route A was conventional rolling since the warm rolling direction in

both stages was the same as the HRD, and this was used as a benchmark for comparison. The other three routes all involved cross rolling, but with alternative rolling directions (HRD or HTD) in the two stages. The final thin sheets after warm rolling were annealed at 1000 °C for 10 min in 100% nitrogen atmosphere.

The microstructure, microtexture and macrotexture were characterized by optical microscopy (OM), electron backscatter diffraction (EBSD) and X-ray diffraction (XRD), respectively. The OM samples were prepared using standard metallographic procedures and etched with a solution consisting of 5 g copper sulfate, 25 ml hydrochloric acid and 25 ml water. The EBSD samples were prepared by electrolytic polishing. Cross-section areas (RD-ND) were scanned using a Zeiss Ultra 55 scanning electron microscope (SEM) equipped with an Oxford HKL Chanel 5 EBSD system. The grain sizes of the OM samples were measured by a linear intercept method (ASTM E112-13). The macrotexture (XRD) was measured on both the surface and the middle-thickness plane of the sheets. A Bruker D8 Discover X-ray Diffractometer with a Co X-ray source was used to measure three incomplete pole figures, i.e., {110}, {200} and {211}. The orientation distribution functions (ODFs) were calculated using a series expansion method ( $l_{max} = 22$ ). All the texture measurements (including XRD and EBSD) were referred to the RD, TD, and ND where the samples were finally produced, i.e., the cross-rolled samples were referred to the crossing rolling RD and TD, not the original HRD and HTD.

The magnetic properties were measured by a single sheet tester. The dimensions of the test strips were 85 mm × 25 mm (length × width). Magnetic field intensities of 800, 2000, and 5000 A/m at a frequency of 50 Hz were applied to measure the magnetic flux density  $B_8, B_{20}, B_{50}$ , respectively. Core losses (1.0 T) at 50 Hz, 400 Hz, and 1000 Hz ( $P_{10/50}, P_{10/400}, P_{10/1000}$ ) were also recorded. For each warm rolling route, magnetic property tests were conducted along both the RD and TD, and the average magnetic flux density and core loss from both directions were then calculated and compared.

## Results

### Microstructure and texture of the hot band

The cross-section (RD-ND) microstructure of the hot band is shown in Fig. 2a. There is apparent inhomogeneity in the microstructure across the thickness, i.e., the surfaces are composed of fine equiaxed grains due to dynamic/static recrystallization, while the center consists of large elongated grains due to deformation. The sub-surfaces, i.e., transition regions (marked with dashed lines in Fig. 2a), are composed of both elongated and recrystallized grains. Similarly, the textures of the different regions also show apparent discrepancies (Figs. 2b–d). The surfaces exhibit a moderate brass ( $\{110\} < 112 >$ ) texture and a near-copper texture ( $\{113\} < 332 >$ ) (Fig. 2b), while the transition regions have similar textures ( $\{110\} < 114 >$  and  $\{112\} < 243 >$ ) but with stronger intensities (Fig. 2c). The central region illustrates a strong  $\theta$ -fiber ( $< 100 > // ND$ ), a moderate  $\alpha$ -fiber

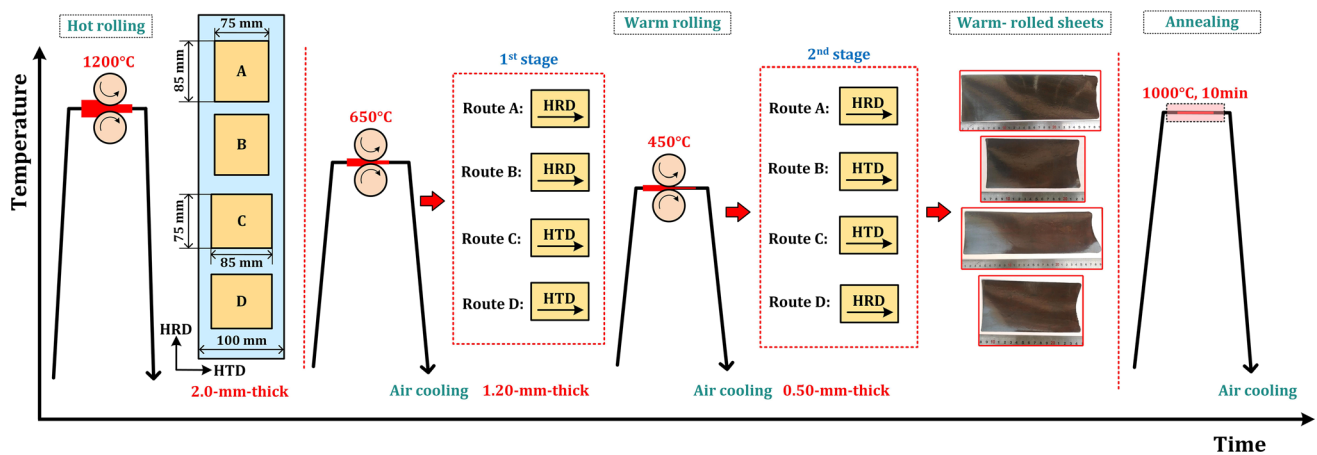
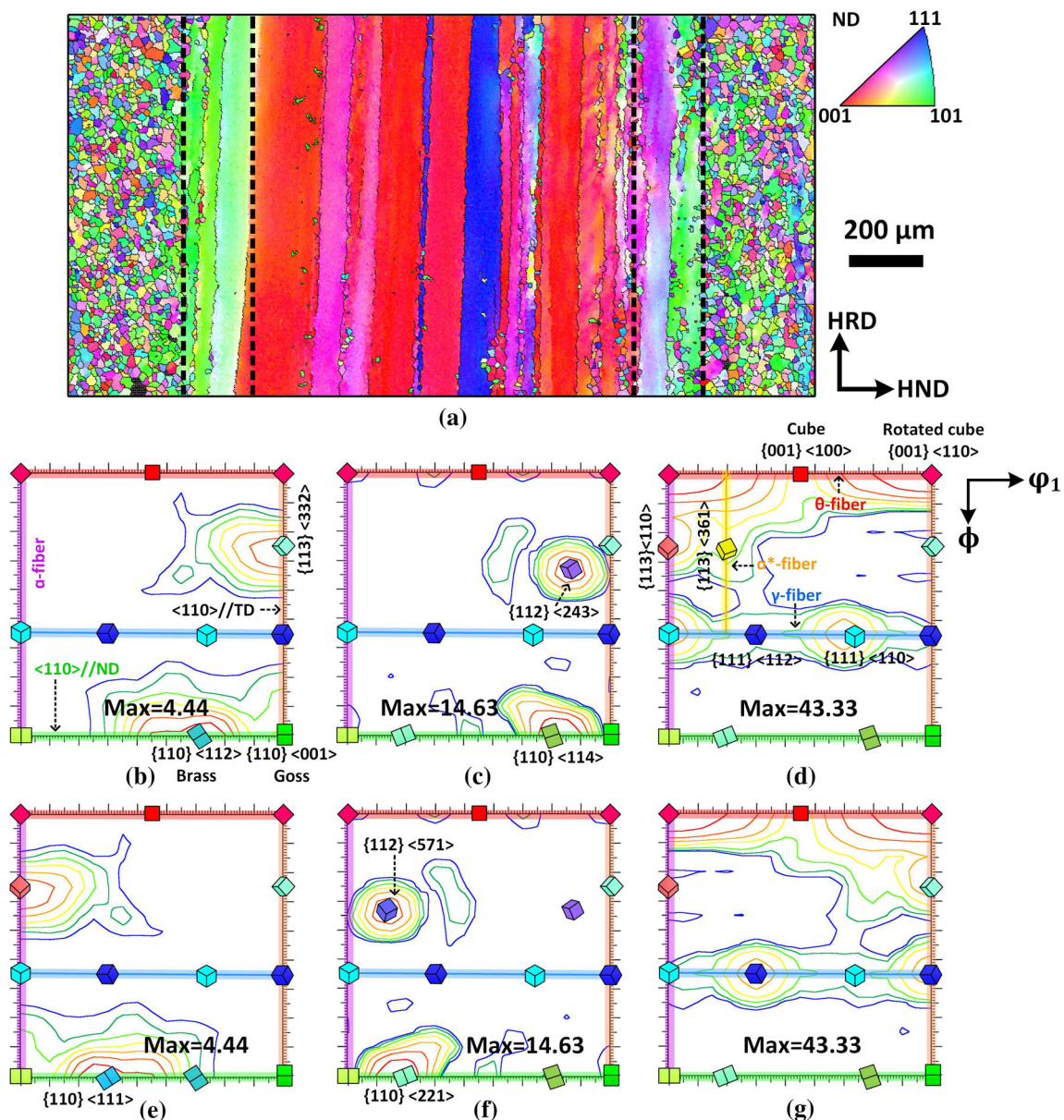


Figure 1 Scheme of the two-stage warm cross rolling process.

and a weak  $\gamma$ -fiber (Fig. 2d). These textures are the initial textures for warm rolling Routes A and B, since the rolling direction of the first-stage warm rolling for these routes is the same as the HRD.

For Routes C and D, because the rolling direction is changed to HTD, the initial textures are rotated 90° around HND (hot normal direction), as shown in Figs. 2e–g. Apparently, the simple rotation results in considerably different textures, especially on the surface and transition regions. The initial

$\{110\} \langle 112 \rangle$  and  $\{110\} \langle 114 \rangle$  components are rotated to  $\{110\} \langle 111 \rangle$  and  $\{110\} \langle 221 \rangle$ , respectively, while the  $\{113\} \langle 332 \rangle$  and  $\{112\} \langle 243 \rangle$  are rotated to  $\{113\} \langle 110 \rangle$  and  $\{112\} \langle 571 \rangle$ , respectively. The 90° rotation around HND essentially does not change the  $\langle 100 \rangle$  //ND fiber in the central region, but it transforms the  $\{111\} \langle 110 \rangle$  on the  $\gamma$ -fiber into the  $\{111\} \langle 112 \rangle$ , and the  $\{113\} \langle 110 \rangle$  on the  $\alpha$ -fiber into the  $\{113\} \langle 332 \rangle$  on the  $\langle 110 \rangle$  //TD fiber. The  $\langle 110 \rangle$  //TD fiber contains a copper



**Figure 2** Microstructure and microtexture of the initial hot band: **a** inverse pole figure (IPF) map of the HND-HRD cross section, **b**, **c**, and **d** textures of the surface, transition, and central regions,

respectively, **e**, **f**, and **g** the corresponding textures after rotating 90° around HND.  $\phi_2 = 45^\circ$  ODF sections of Euler space (Bunge notation).

component ( $\{112\} \langle 111 \rangle$ ) which usually forms in the surface layer after conventional hot rolling of bcc steel [18, 19].

### Microstructure and texture after first-stage warm rolling

The microstructures of the steel after first-stage warm rolling (650 °C) are shown in Fig. 3. Since the rolling direction of Routes A and B is the same as HRD, the microstructure obtained (Fig. 3a) represents that after conventional rolling. It is seen that the microstructure shows apparent differences across the thickness, i.e., small grains at the surfaces (originated from the initially fine and equiaxed grains in the hot band, but with some deformation), and large elongated grains with numerous *slip traces* (forming a net shape) at the center. These traces are not *shear bands* as will be shown later in the Discussion section. It is also noted that between the surface and central regions, there is a transition region also with elongated grains, but the etching color is lighter than the central region, indicating less deformation in these grains. As shown in Fig. 2a, the transition regions are mainly composed of  $\{112\} \langle 243 \rangle$  and  $\{110\} \langle 114 \rangle$  grains, which have higher Taylor factors (under plane-strain compression) than the center grains (mostly  $\langle 100 \rangle // \text{ND}$  orientations) [20–22]; thus, they have higher resistance to deformation.

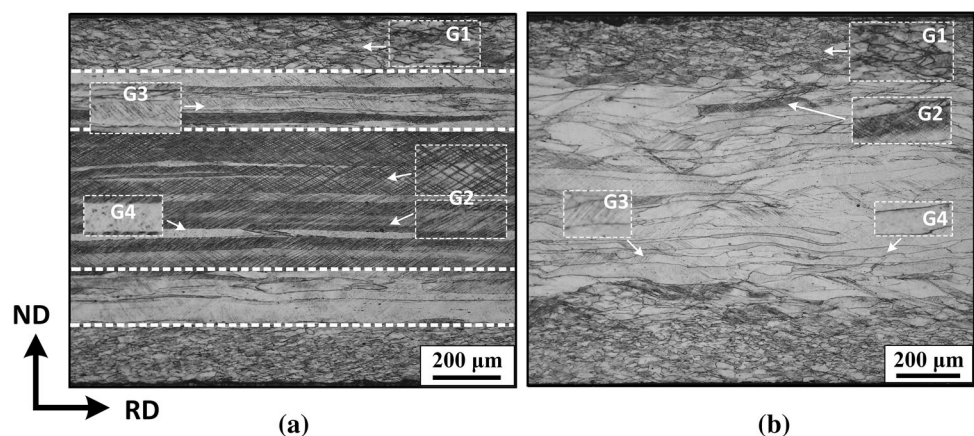
The samples after first-stage *cross rolling* (Routes C and D) show a significantly different microstructure, especially at the central region (Fig. 3b). Due to the change in the rolling direction from HRD to HTD, the central region shows much lighter etching color, and the net-shaped slip traces formed in *conventional rolling* (Fig. 3a) are not obvious in these samples. The

transition regions observed in the conventionally rolled samples are not seen in these samples. Apparently, the rotation of the initial texture by 90° around the HND changed the slip behavior of the grains during deformation, which resulted in the apparent difference in the deformation microstructure.

The deformation textures after first-stage warm rolling are shown in Figs. 4a–d. For both conventional rolling (Routes A and B) and cross rolling (Routes C and D), the surface textures are very weak, while the textures at the central layers are extremely strong. A common feature of the central texture of both rolling routes is that the continuous  $\gamma$ -fiber (commonly observed in cold-rolled electrical steel) is significantly weakened. Although in both cases, the main texture at the central layer is the rotated cube ( $\{100\} \langle 011 \rangle$ ), the cross-rolled samples (C and D) show a much higher intensity than that of conventionally rolled samples (A and B), i.e., 166 vs. 72. There is a relatively strong  $\{111\} \langle 112 \rangle$  component (intensity 18.75) in the cross-rolled samples, but essentially no  $\langle 111 \rangle // \text{ND}$  texture is seen in the conventionally rolled samples. Samples A and B show a strong  $\alpha$ -fiber, while there is no  $\alpha$ -fiber in the cross-rolled samples.

Depending on the rolling direction (either HRD or HTD) in the second-stage warm rolling, the textures after first-stage warm rolling may be rotated 0° or 90° around the HND, which gives rise to the starting textures for the second-stage warm rolling (Figs. 4e–l). Apparently, even after 90° rotation, the main textures (central layer) for all the cases are still the rotated cube ( $\{100\} \langle 011 \rangle$ ). For the sample after first-stage conventional rolling and to be rolled in HTD in the second stage (Route B), the original very strong  $\alpha$ -fiber ( $\langle 110 \rangle // \text{RD}$ ) is now transformed

**Figure 3** Microstructures after first-stage warm rolling: **a** Routes A and B (rolling along HRD), and **b** Routes C and D (rolling along HTD).



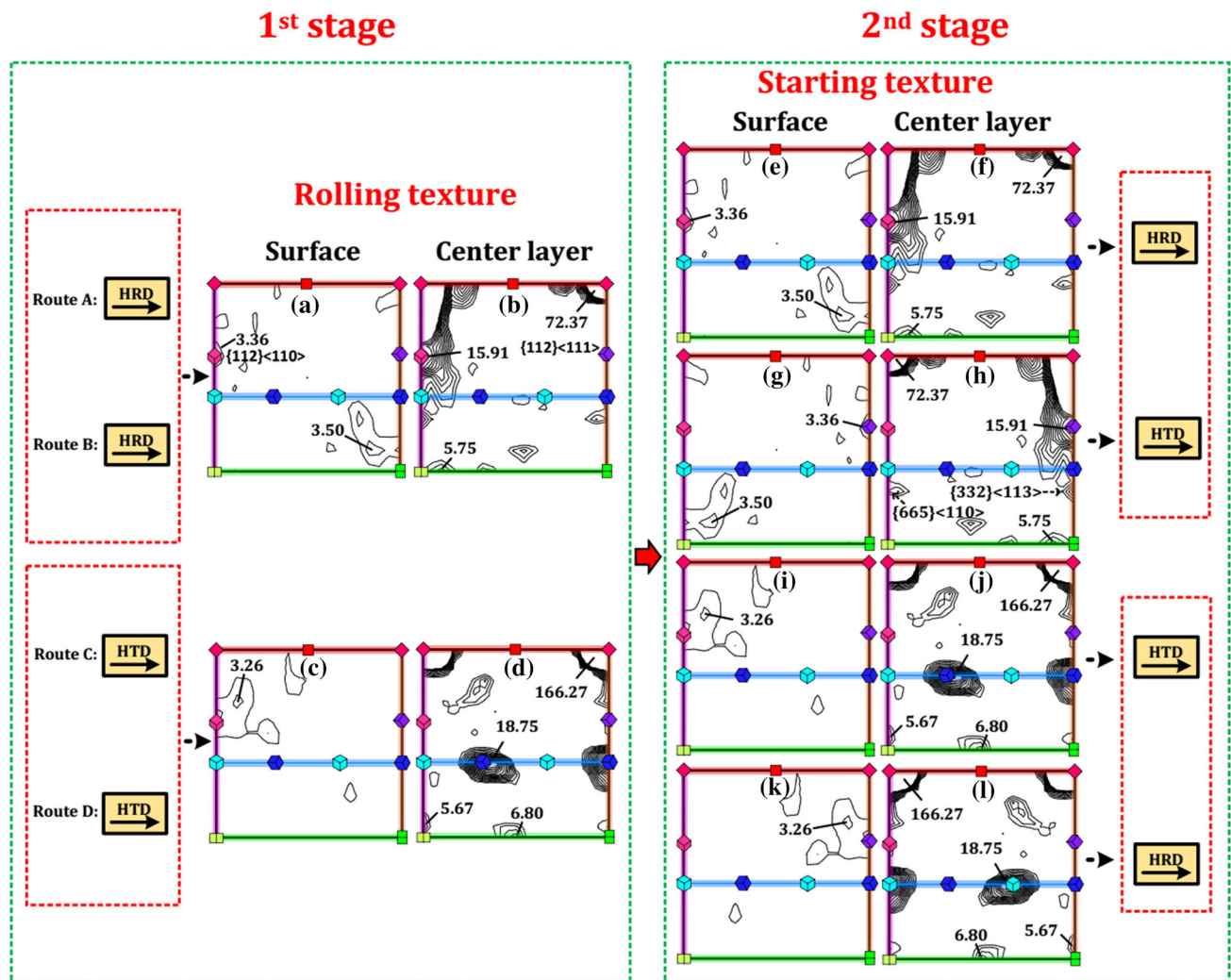


**Figure 4** Macrotextures of the samples after first-stage warm rolling: **a, b** surface and center textures after conventional rolling (Routes A and B), **c, d** surface and center textures after cross rolling (Routes C and D), **e–l** starting textures for second-stage

warm rolling. Note that **g** and **h** are obtained from rotating **a** and **b**, respectively, by  $90^\circ$  around HND, and **k** and **l** are obtained by the same rotation from **(c)** and **(d)**, respectively.  $\varphi_2 = 45^\circ$  ODF sections of Euler space (Bunge notation).

into the  $\langle 110 \rangle // \text{TD}$  texture after  $90^\circ$  rotation around HND. On the other hand, the  $90^\circ$  rotation from HTD to HRD (Route D), brings the original  $\{111\} \langle 112 \rangle$  texture to the  $\{111\} \langle 110 \rangle$ .

### Microstructure and texture after second-stage warm rolling

The microstructures after second-stage warm rolling are shown in Fig. 5. All the four samples consist of small, deformed grains at the surfaces and large, elongated grains in the center layer. The etching color in the center region is lighter in Samples B, C, and D than in Sample A, due to the change in the rolling

direction either in the first stage or in the second stage, which has resulted in different slip activities during deformation. The net-shaped slip traces observed in Sample A after first-stage warm rolling are still visible, but the amount has been significantly reduced. No such structure is observed in Samples B, C, and D. While Samples A, C, and D still show elongated grains (parallel to RD) in the central region as in the hot band (Fig. 2a), the deformed grains in the central region of Sample B essentially do not show such elongated structure.

The macrotextures after second-stage warm rolling are shown in Fig. 6. Again, the textures at the surfaces of all the samples are very weak, while those at

the central layers are extremely strong. Both Samples A and D are rolled in the HRD during second-stage warm rolling, so their surface textures are quite similar to each other, which are also similar to typical rolling textures (with  $\alpha$ - and  $\gamma$ -fibers) [23, 24]. The surface textures of Samples B and C (rolled in HTD in the second-stage warm rolling) are quite weak, with some peaks on the  $\alpha$ -fiber. It should be noted that there is essentially no  $\gamma$ -fiber in the surface texture of Sample B, but a weak  $\gamma$ -fiber is seen in the surface texture of all the other samples.

The central layer textures show significant differences among the four samples. Compared to conventional rolling (Route A), the change in rolling direction from the original HRD to HTD during warm rolling, either in the first stage (D) or the second stage (B), or both (C), significantly increases the maximum texture intensity, i.e., from 40.83 to 96.74–144.60. Although the major texture component is still rotated cube in all the cases, a major difference between conventional rolling (A) and cross rolling (B, C, D) is that there is a strong  $\alpha$ -fiber in conventional rolling, while this texture has been completely eliminated by cross rolling. The strong  $\alpha$ -fiber in conventionally warm rolled sample (A) is inherited from the first-stage warm rolling (Fig. 4b) and is strengthened by the second-stage rolling. If the

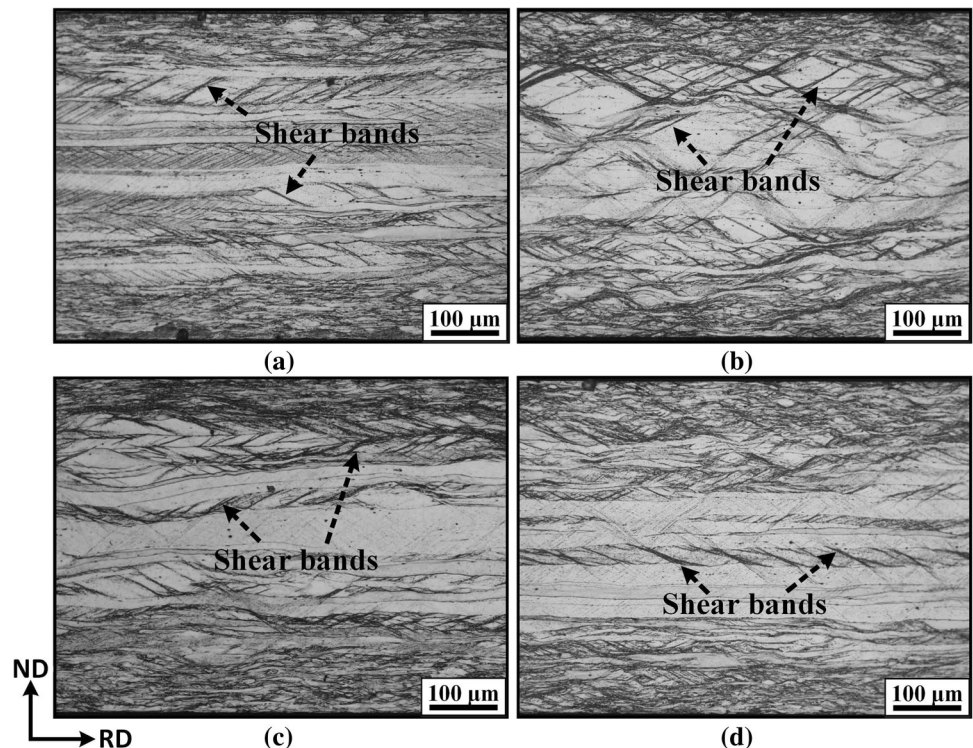
rolling direction in both stages is HTD (C), the  $\{111\} < 110 >$  is very weak. In all the other cases, the  $\{111\} < 110 >$  component is relatively strong. It is thus seen that, rolling along the HRD, either in the first stage (B) or second stage (D), or both (A), is necessary to produce the  $\{111\} < 110 >$  texture. In other words, warm rolling in the HTD can essentially eliminate the  $\{111\} < 110 >$  texture (C).

Route B shows the strongest texture with a maximum intensity of 144.60. Apparently, keeping the rolling direction in HRD in the first stage and changing it to HTD in the second stage has resulted in such a strong texture; the opposite change in rolling directions, i.e., from HTD to HRD (Route D) does not lead to such a strong texture. If the starting textures of these two samples are compared (Figs. 4h, l), Route D even shows a much stronger initial texture than Route B, but after the two-stage warm rolling, Route B shows a much stronger texture than Route D. Thus, the change in the rolling direction during the two-stage warm rolling does have a significant effect on the final deformation texture.

### Microstructure and texture after annealing

The cross-section (RD-ND) microstructures of the annealed samples are shown in Figs. 7a-d. It is seen

**Figure 5** Optical micrographs after second-stage warm rolling: **a** Route A, **b** Route B, **c** Route C, **d** Route D.



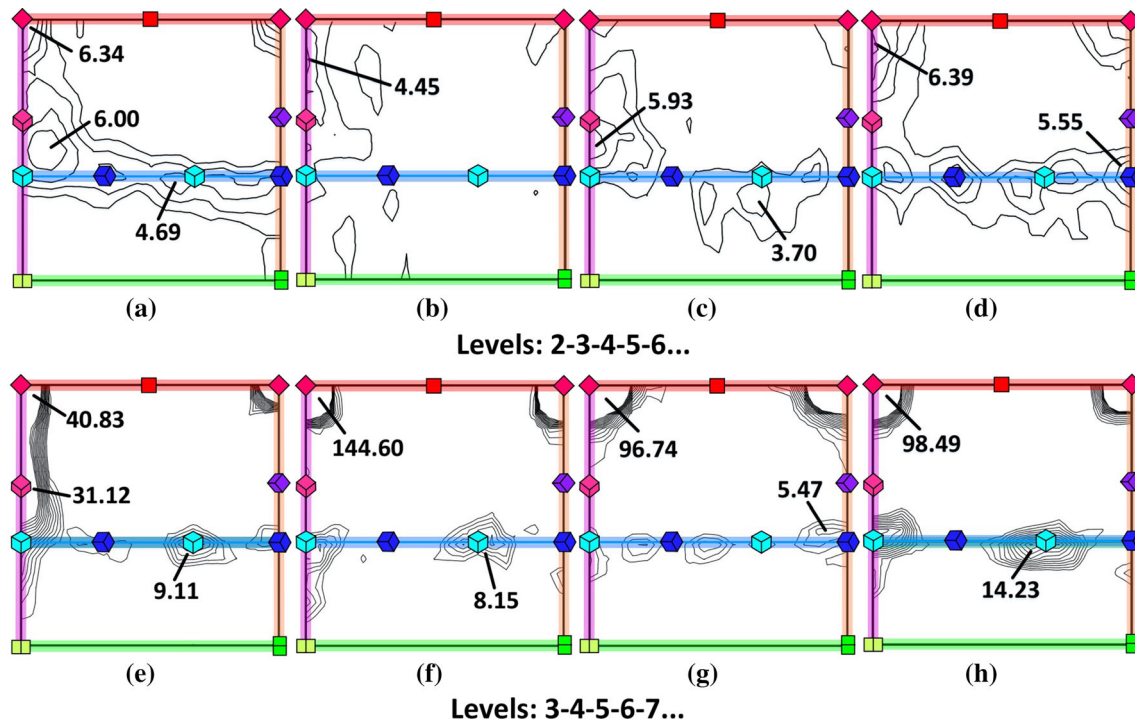


**Figure 6** Macrot textures after second-stage warm rolling: **a**, **b**, **c**, and **d** surface textures for Routes A, B, C, and D, respectively, **e**, **f**, **g** and **h** textures of the center layer for Routes A, B, C, and D, respectively.  $\varphi_2 = 45^\circ$  ODF sections of Euler space (Bunge notation).

that the layered structures after warm rolling (Fig. 5) are somewhat retained since the annealed samples also show apparent layered clusters of grains with similar colors. Samples A, C, and D illustrate more obvious banded structures than Sample B, which is because the original deformed structures of these samples are composed of more clearly delineated elongated grains than Sample B (Fig. 5). Two main colors can be noticed in the inverse pole figure (IPF) maps, i.e., red ( $\langle 100 \rangle // \text{ND}$ ) and blue ( $\langle 111 \rangle // \text{ND}$ ). The  $\langle 100 \rangle // \text{ND}$  grains are mainly located in the center region, which are originated from the elongated  $\langle 100 \rangle // \text{ND}$  grains after warm rolling (Fig. 5). The  $\langle 111 \rangle // \text{ND}$  grains are mostly distributed near the surface regions where the microstructure is originally composed of numerous small recrystallized grains with small deformation (elongation) after warm rolling.

The average grain areas of the samples after annealing are shown in Fig. 7e. The grain areas show some moderate variations, i.e., Samples A and C (rolling direction did not change between the two stages) have larger average grain areas and larger standard deviations than Samples B and D (rolling direction changed between the two stages). Thus, changing the rolling direction *between* the two stages

(B and D) not only reduces the grain size (area), but also improves the uniformity of the microstructure. Sample B shows the smallest grain size and the most uniform microstructure, while Sample C has the largest grain size.

The macrot textures (XRD) of the samples after annealing are shown in Fig. 8. Compared to the deformation textures shown in Fig. 6, the surface textures (e.g., the  $\gamma$ -fiber) are all strengthened, while the central textures (e.g., rotated cube) are significantly weakened. Sample B shows the weakest surface texture among all the samples after annealing. In the middle-thickness plane, the extremely strong textures after warm rolling (Figs. 6e-h) are significantly randomized after annealing. All samples show a strong  $\{001\} \langle 120 \rangle$  texture which extends to  $\{118\} \langle 8\ 16\ 1 \rangle$  or even  $\{112\} \langle 241 \rangle$  (all are on the  $\alpha^*$ -fiber,  $\{11\ h\} \langle 1\ 2\ 1/h \rangle$ ). Samples A and D (rolling direction in the second stage is HRD) also show a strong  $\alpha$ -fiber and relatively strong  $\{111\} \langle 231 \rangle$  components on the  $\gamma$ -fiber (with intensities of 7.89 and 6.88, respectively), which resembles the textures obtained in previous work [23]. If the rolling direction in the second stage is HTD (Routes B and C), the  $\gamma$ -fiber is essentially eliminated, and the  $\{001\} \langle 120 \rangle$  only extends to



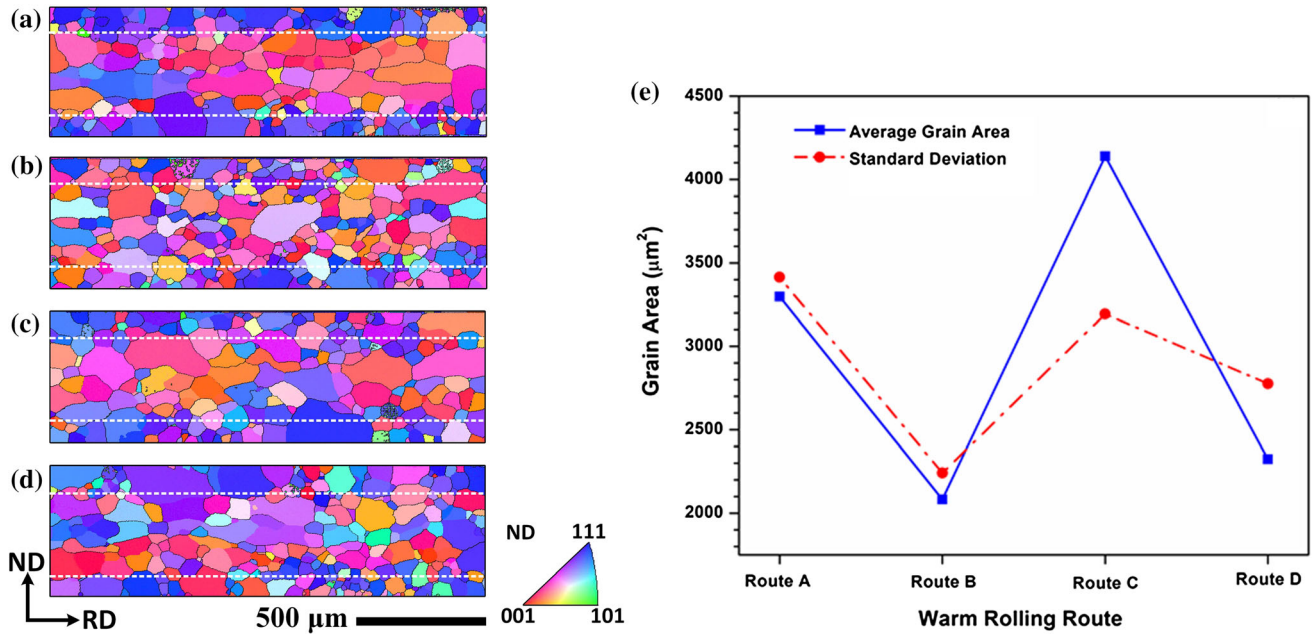


**Figure 7** Microstructure after annealing: IPF maps of **a** Sample A, **b** Sample B, **c** Sample C, **d** Sample D; **e** average grain area and standard deviation.

approximately  $\{118\} \langle 8\ 16\ 1 \rangle$ . A minor cube component is noticed in Sample D, which is not seen in all the other samples. Thus, Routes B and C can optimize the final texture by essentially eliminating the  $\gamma$ -fiber and the  $\alpha$ -fiber.

### Magnetic properties

Figure 9 shows the magnetic properties of the final annealed sheets processed using different warm cross rolling routes. The differences in the average

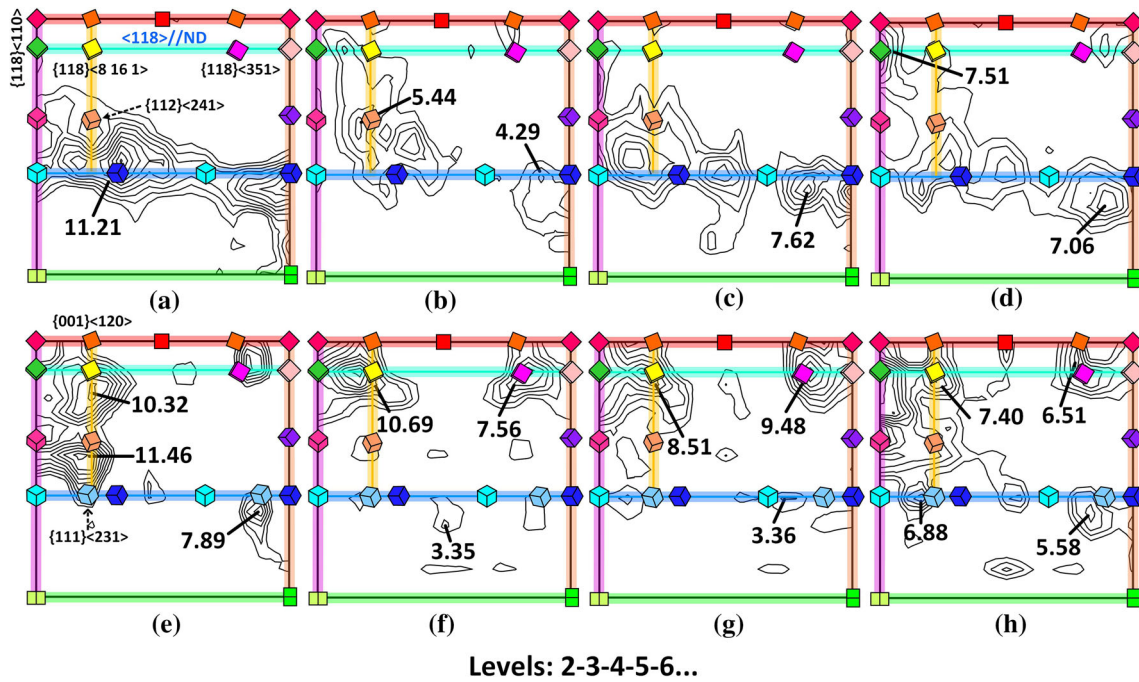


**Figure 8** Macrottextures (XRD) after annealing: **a**, **b**, **c** and **d** surface textures for Samples A, B, C, and D, respectively, **e**, **f**, **g**, and **h** center layer textures for Samples A, B, C, and D, respectively.  $\varphi_2 = 45^\circ$  ODF sections in Euler space (Bunge notation).

magnetic flux density among the different warm rolling routes are very small, i.e., with relative standard deviations (standard deviations divided by the mean values) of only 0.7–1.0% for the different magnetic fields applied. Generally, the magnetic flux density at a frequency of 50 Hz is slightly increased by all the cross-rolling routes (Routes B, C and D), and Route B results in the maximum magnetic flux density at all the magnetic fields applied, i.e., 1.37 T, 1.45 T, and 1.56 T for  $B_8$ ,  $B_{20}$  and  $B_{50}$ , respectively (Fig. 9a).

The core losses show slightly larger variations among the different routes, i.e., with relative standard deviations of 1.5–3.3% for the different frequencies. The core losses at a peak flux density of 1.0 T show different trends under different frequencies (Fig. 9b). At high frequencies (400 and 1000 Hz), Route D results in the lowest core loss, while at a low frequency (50 Hz), Route C leads to the lowest core loss. On the other hand, when the frequency is 1000 Hz, Route C gives rise to a large increase in core loss. Except for Route C at 1000 Hz and Route B at 50 Hz, the cross-rolling routes also reduce the core losses.

## Discussion

It is well known that the cold rolling textures of bcc metals are normally quite similar regardless of the material, although the chemical composition (e.g., solute addition), the grain size, and the amount of strain may have some effects on the detailed features of the texture. The typical bcc rolling texture consists

of a partial  $\alpha$ -fiber (from  $\{001\} \langle 110 \rangle$  to  $\{111\} \langle 110 \rangle$ ) and a  $\gamma$ -fiber (from  $\{111\} \langle 110 \rangle$  to  $\{111\} \langle 112 \rangle$ ). These textures have been reasonably well predicted by Taylor-type models implying different slip planes, i.e.,  $\{110\}$ ,  $\{110\} + \{112\}$ , or  $\{110\} + \{112\} + \{123\}$  [25].

The main alloying element in electrical steel is silicon, which forms a substitutional solid solution in the iron lattice [26]. Since the crystal structure is still bcc, the addition of silicon is expected to have limited effect on the cold rolling texture. If the silicon content is up to  $\sim 3.5$  wt%, the cold rolling texture is usually very similar to that of low carbon steel. Nevertheless, it has been considered [27] that silicon reduces the number of active slip systems (less cross slip activity because of lower stacking fault energy) at low temperatures, leading to concentrated crystal orientations. The appearance of a  $\{111\} \langle 110 \rangle$  component instead of a continuous  $\gamma$ -fiber in the conventionally warm rolled steel (Fig. 6e) may be attributed to this. On the other hand, it has been reported [28] that homogeneous deformation twinning (under tension) occurs in columnar-grained 6.5 wt% Si steel at intermediate temperatures. This deformation mode may also be expected to operate during warm rolling of high silicon steel, which may influence the texture as well. However, the dominant deformation mode in high silicon steel is still slip.

It has been shown that the main factors influencing the bcc rolling texture include the starting texture, the types of potential slip systems, and the constraints imposed by the neighboring grains [25, 29]. The warm cross-rolling scheme applied in this study imposed several different conditions on the material

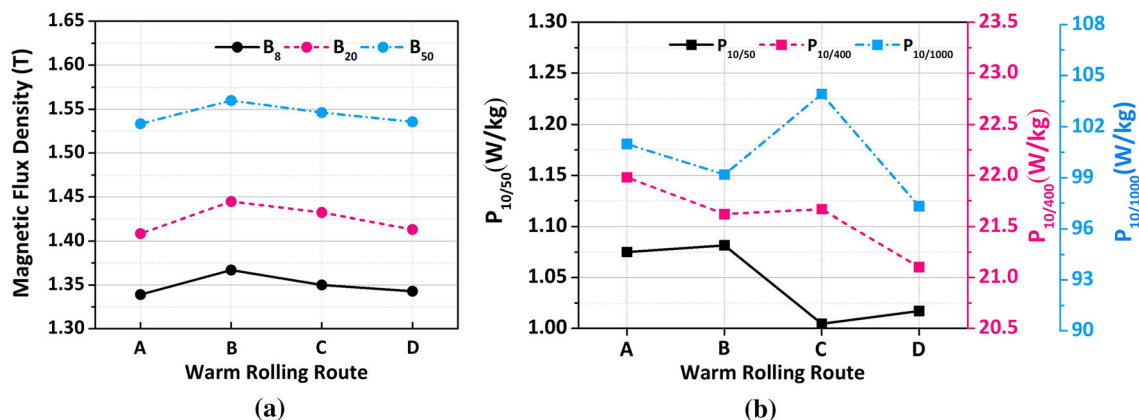


**Figure 9** Magnetic properties of the steel after final annealing: **a** magnetic flux densities at 800 A/m, 2000 A/m, and 5000 A/m magnetic fields (frequency 50 Hz), **b** core losses (1.0 T) at 50 Hz, 400 Hz, and 1000 Hz.

as compared to conventional cold rolling. First, it was deformed at elevated temperatures, which was associated with dynamic recovery of the material during the deformation (e.g., dislocation climb, cross slip and glide, etc.). At higher temperatures, the critical resolved shear stress and the work hardening rate were lower than cold rolling; thus, it was possible to activate more slip systems and/or different slip systems during warm deformation. Second, the initial texture before warm rolling was changed (rotated 90° around ND), which led to different crystal orientations (and dislocation configurations) and thus different active slip systems under the same deformation mode. Third, the constraints imposed by the neighboring grains were also changed due to the changes in their orientations with respect to the new reference frame. All these contributed to the variations in the deformation texture and microstructure after different routes of warm cross rolling, which led to different final textures after annealing.

### Formation of slip bands after conventional warm rolling (650 °C)

It has been shown in Fig. 3a that, numerous dark-etched, net-shaped slip traces were observed in the central region (middle thickness) of the steel after *conventional* warm rolling at 650 °C. This kind of deformation structure was not frequently observed in cold-rolled or hot-rolled electrical steels, or in warm *cross-rolled* sample at the same temperature (Fig. 3b). These slip traces (lines or bands) were initially thought as shear bands, but EBSD scans on these regions confirmed that these were *slip bands* instead of shear bands.

Slip bands are clusters of slip lines left on the (polished) surface of deformed metal due to slip along the slip direction on the slip plane. These correspond to *microbands* as observed in conventional microstructure analysis of deformed metals [30]. Very small orientation change is expected at the boundaries between the slip bands and the crystal matrix (less than  $\sim 2.5^\circ$  as revealed by EBSD in this study). On the other hand, shear bands are narrow regions of intense shear resulted from local plastic instability (inhomogeneous deformation) [31], which contain very fine and highly misoriented dislocation cells [32]. Thus, there are large local orientation changes at the borders between the shear bands and the crystal matrix.

As shown in Fig. 10a, an EBSD scan across the thickness of the sheet indicates that the crystals in the central region (where the net-shaped structure was observed) could be readily indexed, and there is no apparent orientation variation within the grains. This is fundamentally different from the shear bands where the accumulation of dislocations or the distortion of the lattice normally leads to unable-to-index pixels, and there are well-defined boundaries and apparent orientation changes from the matrix to the shear bands [22, 33–35].

The formation of such slip bands instead of shear bands could be attributed to the relatively high deformation temperature (650 °C) which may have activated additional slip systems (e.g.,  $\{112\} \langle 111 \rangle$  or even  $\{123\} \langle 111 \rangle$ ) in addition to the most common  $\{011\} \langle 111 \rangle$  slip systems. A common result of the activation of multiple slip systems is cross slip, which could have left traces of the slip planes on the surfaces. Figure 10c is an SEM micrograph of the sample after warm rolling (Route A) at 650 °C. The net-shaped slip traces are clearly seen in the enlarged view of two grains. Due to the difference in grain orientation, the slip bands in the upper grain are inclined at  $\sim 30^\circ$  and  $\sim 34^\circ$  to the RD, while the slip bands in the lower grain have inclination angles of  $\sim 20^\circ$ ,  $\sim 25^\circ$  and  $\sim 30^\circ$  to the RD. As shown in Figs. 10d, e, the projection of specific crystallographic planes of a (001)[–210] crystal (a major texture observed in the sample) onto the sample surface illustrates that the angles between the  $\{001\}$  and  $\{112\}/\{123\}$  planes are approximately  $30\text{--}34^\circ$ , which coincide with the angles between the slip bands as observed in the microstructure (Fig. 10c).

### The influence of warm cross-rolling route on the texture evolution

The textures after warm rolling (Fig. 4, 6) showed significant discrepancies between the surface and central regions. The weak surface textures were due to the weak initial textures before warm rolling (after hot rolling, Fig. 2) and to the dynamic/static recrystallization occurring in the surfaces during warm rolling. The central region, on the other hand, had very strong initial textures and the material essentially had only undergone recovery (no recrystallization) during warm rolling; thus, the deformation textures were very strong. Since the surface texture is

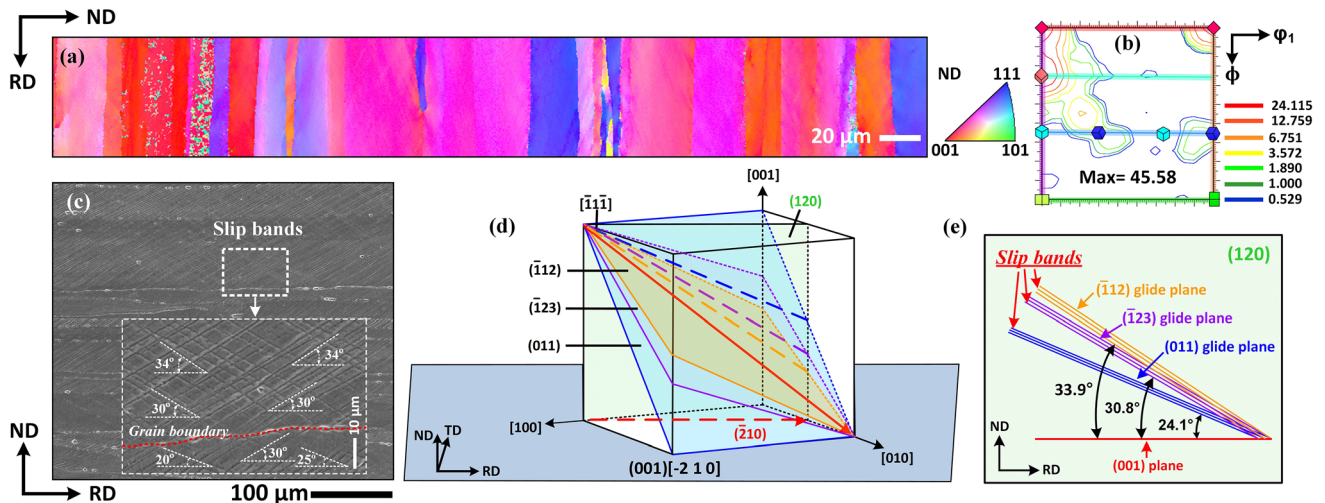


**Figure 10** Slip bands in the sample after first stage warm rolling (Route A): **a** EBSD IPF map showing correctly indexed area with slip bands, **b** the corresponding texture ( $\phi_2 = 45^\circ$  ODF section), **c** SEM micrograph showing slip bands in two grains, **d** slip planes

very weak in all the cases, the discussion on the effect of warm cross-rolling route on texture evolution will be focused on the central layer only.

#### First-stage warm rolling (650 °C)

The first-stage conventional warm rolling at 650 °C (along HRD) significantly strengthened the rotated cube texture (inherited from hot rolling), i.e., the intensity increased from 43.33 (Fig. 2d) to 72.37 (Fig. 4b). The sharpening of this texture has also been reported in low carbon steels during warm rolling [36], and it was attributed to the preferential action of {112} slip [37] and to the reduction in shear flow localization due to the elevated rolling temperature [36]. Senuma et al. [38] reported that the {112} slip could increase the intensities of the {113} < 110 > to {115} < 110 > textures during rolling, which may explain the strong components ranging from {113} < 110 > to {001} < 110 > as observed in Fig. 4b. In addition, it has been shown [39] that the rolling of the < 001 > //ND fiber texture (including the cube) will rotate these orientations towards the {001} < 110 >; thus, the original < 001 > //ND fiber after hot rolling was essentially transferred to orientations close to the rotated cube orientations.

The {112} < 110 > component, which is usually a stable and strong final orientation during cold rolling as predicted by crystal plasticity simulations and also observed in many experiments [12, 40–42], only

in a (001)[-210] crystal with respect to the sample, **e** the projection of the slip planes onto the sample surface showing lines inclined at 24.1°, 30.8° and 33.9° to the RD.

shows a moderate intensity of 15.91 here. It has been shown [43, 44] that cross slip (which is evident during conventional warm rolling as shown above) will enhance the deviation of the texture from {112} < 110 > to {001} < 110 >, which may explain why only a moderate {112} < 110 > is noted in Fig. 4b. Taylor-type simulations [25] have shown that incorporating the {112} slip into the {110} slip will degrade the {111} < 110 > texture. Thus, the activation of the {112} slip during warm rolling sharpens the {001} < 110 > texture and eliminates the {111} < 110 > texture.

The {111} < 112 > texture is known to be a stable orientation during cold rolling [45], but at elevated temperatures, contradictory results have been reported. Senuma et al. [38] reported a decreased {111} < 112 > texture during rolling at elevated temperatures and attributed the decrease to the preferential {112} slip. Barnett [36], on the other hand, observed an increase in the intensity of this texture during warm rolling of low carbon steels, due to the reduced fragmentation and shear banding formation at high temperatures. The elimination of the {111} < 112 > during *conventional* warm rolling observed in this study seems to be in line with the observations of Senuma et al. [38]. However, as shown below, the results for the warm *cross-rolled* sample seem to contradict this.

After first-stage warm *cross* rolling (Fig. 4d), the texture was enormously intensified, i.e., the

maximum intensity (rotated cube) increased to 166.27, and the texture essentially only consisted of two orientations:  $\{001\} \langle 110 \rangle$  and  $\{111\} \langle 112 \rangle$ . It has been shown that the  $90^\circ$  rotation around the ND transferred the partial  $\alpha$ -fiber and the  $\{111\} \langle 110 \rangle$  (Fig. 2d) to the partial  $\langle 110 \rangle // \text{TD}$  fiber and the  $\{111\} \langle 112 \rangle$ , respectively (Fig. 2g), but the same rotation did not change the  $\langle 001 \rangle // \text{ND}$  fiber due to crystal symmetry. It has been reported [12, 46] that the  $\langle 110 \rangle // \text{TD}$  orientations (rotated from the  $\langle 110 \rangle // \text{RD}$ ) are unstable and tend to rotate to  $\{001\} \langle 110 \rangle$  or  $\{111\} \langle 112 \rangle$  depending on the sheet normal direction: a sheet normal close to  $\langle 001 \rangle$  will give rise to a  $\{001\} \langle 110 \rangle$ , while those between  $\langle 111 \rangle$  and  $\langle 110 \rangle$  will lead to a strong  $\{111\} \langle 112 \rangle$ . The initial texture shown in Fig. 2g had a strong  $\langle 110 \rangle // \text{TD}$  texture with sheet normal close to  $\langle 001 \rangle$ ; thus, the rolling of this texture significantly strengthened the  $\{001\} \langle 110 \rangle$  texture. The extremely high intensity (166.27) of the rotated cube was mainly due to the rolling of the unstable  $\langle 110 \rangle // \text{TD}$  components, which were absent during conventional rolling. Kestens and Jacobs [12] also reported such a high intensity (156) of rotated cube in cross-rolled electrical steel. Again, the original weak  $\{111\} \langle 110 \rangle$  texture was degraded due to the preferential  $\{112\}$  slip, as discussed above. The  $\{111\} \langle 112 \rangle$  texture (intensity 18.75), on the other hand, was inherited from the original  $\{111\} \langle 112 \rangle$  texture (rotated from the  $\{111\} \langle 110 \rangle$ , Fig. 2g), which was believed to be “stabilized” because of its high Taylor factor, as explained by Barnett [36].

### Second-stage warm rolling (450 °C)

Depending on the rolling direction in the second-stage warm rolling, the texture may be weakened or strengthened. The texture after second-stage *conventional* warm rolling (Route A, Fig. 6e) is very similar to the initial texture (Fig. 4f), i.e., mainly consisting of a rotated cube and an  $\alpha$ -fiber. However, the maximum intensity ( $\{001\} \langle 110 \rangle$ ) decreased from 72.37 to 40.83. This is because the rotated cube grain (very strong after first-stage warm rolling) has a low Taylor factor and can be readily deformed and rotated during rolling (fragmented and forming deformation bands, etc.). At this temperature, the activation of the  $\{112\}$  slip is low because the transition of slip plane from  $\{110\}$  to  $\{112\}$  increases with temperature [47]. In

addition, the high silicon content in the steel also reduces the tendency for cross slip (due to low stacking fault energy) [27]. Thus, the slip at lower temperatures is mainly on  $\{110\}$  plane, which usually leads to the rotation of the  $\{001\} \langle 110 \rangle$  towards the  $\{112\} \langle 110 \rangle$ , as predicted by crystal plasticity simulations [25]. On the other hand, the  $\alpha$ -fiber in the initial texture is strengthened by further increasing the rolling reduction during the second-stage conventional warm rolling.

The texture of this sample also contains a  $\{111\} \langle 110 \rangle$  component (intensity 9.11) on the  $\gamma$ -fiber, which is not present in the initial texture (after first-stage warm rolling, Fig. 4b). This component may have come from the further deformation of the  $\{112\} \langle 110 \rangle$  orientation (on the  $\alpha$ -fiber), which rotates to the  $\{111\} \langle 110 \rangle$  during plane-strain compression [39]. It may also have come from the near- $\{111\} \langle 112 \rangle$  orientations (e.g.  $\{332\} \langle 113 \rangle$ ) since it has been shown [40, 45, 48] that the rolling of  $\{111\} \langle 112 \rangle$  can also lead to the  $\{111\} \langle 110 \rangle$ .

If the rolling direction of the second-stage warm rolling is changed to HTD (Route B), the rotated cube texture is significantly strengthened, i.e., the intensity increases from 72.37 to 144.60, which is opposite to Route A where the maximum intensity decreased from 72.37 to 40.83. The main reason for the sharpening of this texture is the rotation of the unstable  $\langle 110 \rangle // \text{TD}$  texture (obtained from  $90^\circ$  rotation of the  $\alpha$ -fiber after first-stage warm rolling) to the  $\{001\} \langle 110 \rangle$  during further rolling, as discussed above. The formation of the  $\{111\} \langle 110 \rangle$  component (intensity 8.15, Fig. 6f) may be related to the rotation of the initially discrete components near the  $\{111\} \langle 110 \rangle$  (e.g.,  $\{665\} \langle 110 \rangle$ ), in the initial texture (Fig. 4h).

Compared to conventional warm rolling (Route A), where further rolling of the rotated cube in the same direction (HRD) rotates it towards  $\{112\} \langle 110 \rangle$  and strengthens the  $\alpha$ -fiber (Fig. 6e), none of the cross rolling routes (B, C or D) forms an  $\alpha$ -fiber after second-stage warm rolling (Figs. 6f–h), although the initial rotated cube texture after first-stage warm rolling is also very strong. It is noted that due to the  $90^\circ$  rotation around ND (either in the first stage, Routes C and D, or in the second stage, Route B), no  $\alpha$ -fiber exists in the initial texture. The result is that the final texture does not have an  $\alpha$ -fiber. One explanation is that, theoretically, only crystals with the  $\langle 001 \rangle // \text{ND}$  orientations remain unchanged

after 90° rotation around the ND (due to the fourfold symmetry). All the other orientations will be altered after rotation. Thus, although the change in the rolling direction from HRD to HTD will *not* alter the active slip systems of the  $\langle 001 \rangle // \text{ND}$  grains (including the rotated cube), it will change those of all the other crystals. This means that the deformation of the rotated cube grains will be different from conventional rolling since the local stress distributions (induced by the constraints of neighboring grains) are different. As a result, the expected spread of the  $\{001\} \langle 110 \rangle$  to  $\{112\} \langle 110 \rangle$  in conventional rolling is not seen in cross rolling.

The initial textures of Routes C and D after first-stage warm rolling (Figs. 4j, l) are very similar (except that one has a  $\{111\} \langle 112 \rangle$  and the other has a  $\{111\} \langle 110 \rangle$  component); thus, the textures after second-stage warm rolling are also very similar. The very strong rotated cube is significantly weakened, i.e., the maximum intensity decreases from 166.27 to 96.74/98.49, which can be attributed to the rotation of the rotated cube to other orientations (instead of  $\alpha$ -fiber) during further rolling. The weakening of both the  $\{111\} \langle 112 \rangle$  in Route C (from 18.75 to 5.47) and the  $\{111\} \langle 110 \rangle$  in Route D (from 18.75 to 14.23) can be ascribed to the grain split-up, generation of new high-angle boundaries, and formation of banded structures [36, 49, 50] in grains with high Taylor factors (e.g.,  $\{111\} \langle 112 \rangle$  and  $\{111\} \langle 110 \rangle$ ). All of them will weaken the deformation texture.

To summarize, the above analysis on deformation texture after warm rolling showed that both the initial texture (changed by cross rolling) and the activation of new slip systems (changed because of different deformation temperatures) had effects on the deformation texture. The activation of the  $\{112\}$  slip was apparent during the first stage of warm rolling (650 °C), and both the initial texture and the activation of the  $\{112\}$  slip contribute to the formation of different deformation textures. During the second-stage warm rolling (450 °C), no direct evidence supports the activation of the  $\{112\}$  slip. Thus, the change in the initial texture is the main reason for the different deformation textures produced.

### Annealing

If the *surface* textures after annealing (Figs. 8a–d) are compared to those after warm rolling (Figs. 6a–d), it is seen that the main features of the warm rolling

textures have been inherited after annealing, and in all the cases the textures are also intensified, which is opposite to the conventional trend, i.e., recrystallization usually randomizes the texture. This is because the surface microstructure after warm rolling is essentially composed of small equiaxed grains (with some deformation and recovery) inherited from the hot rolling microstructure. Since the final deformation was conducted at an elevated temperature (450 °C) and the deformation was not large (58% thickness reduction), the microstructure after warm rolling had much less dislocation accumulation and lower stored energy (due to dynamic recovery) than that after cold rolling. As a result, during the subsequent annealing, it is difficult to form new grains (nucleation) from the deformed microstructure. The recrystallization is thus dominated by the growth of the existing grains. Thus, most of the existing textures are inherited and intensified after annealing. However, the rotated cube is eliminated (Routes A, B, and C) or weakened (Route D) after annealing. This might be due to the higher stored energy of the rotated cube than that of the  $\gamma$ -fiber in the surface (the deformation in the surface is mainly shearing instead of plane-strain compression) [51], which results in the consumption of the rotated cube by the  $\gamma$ -fiber during grain growth.

In the *center* region, the warm rolling microstructure was composed of deformed grains, and the texture was mainly rotated cube (with very high intensity). Upon annealing, new grains nucleate and grow, and consume the deformed matrix; thus, the very strong deformation texture is significantly randomized, i.e., maximum intensities drop from 40.83–144.60 to 7.40–11.46. It has been shown (Figs. 8e–h) that the main recrystallization textures in all the cases are  $\{001\} \langle 120 \rangle // \{118\} \langle 8\ 16\ 1 \rangle // \{114\} \langle 481 \rangle$  (all on the  $\alpha^*$ -fiber), and Routes A and D also show an extended  $\alpha^*$ -fiber to  $\{111\} \langle 231 \rangle$  on the  $\gamma$ -fiber.

A major feature of the textures of all the samples after second-stage warm rolling is the elimination of the  $\langle 111 \rangle // \text{ND}$  fiber texture (only weak discrete orientations are observed). As a result, the nucleation of the  $\gamma$ -fiber texture from the deformed  $\langle 111 \rangle // \text{ND}$  fiber can be essentially neglected. Consequently, the recrystallization texture barely contains a  $\gamma$ -fiber component since the annealed  $\gamma$ -fiber texture is mainly nucleated from the deformed  $\gamma$ -fiber grains [52]. An exception is Route D, which shows a

relatively strong  $\{111\} \langle 231 \rangle$  component because of a relatively strong  $\{111\} \langle 110 \rangle$  after second-stage warm rolling (Fig. 6h).

The formation of the recrystallized  $\alpha^*$ -fiber texture (especially the  $\{113\} \langle 361 \rangle$  and  $\{114\} \langle 481 \rangle$  components) in steel has been reported by several researchers [53–55], but the formation mechanism for this texture is still under debate. Nevertheless, it is generally accepted that the existence of a strong rotated cube or a  $\langle 110 \rangle // \text{RD}$  ( $\alpha$ -fiber) texture in the deformed microstructure is necessary for the formation of the  $\{113\} \langle 361 \rangle$  and  $\{114\} \langle 481 \rangle$  components [53]. It is also believed that the oriented nucleation of these components from the deformed  $\alpha$ -fiber (e.g., rotated cube) grains is responsible for the formation of the final  $\alpha^*$ -fiber texture [53]. Since in this study all the samples after warm rolling have a very strong rotated cube texture, it is not surprising to observe the  $\alpha^*$ -fiber texture in the recrystallized microstructure. However, it should be noted that the previously reported  $\alpha^*$ -fiber recrystallization textures were mostly  $\{113\} \langle 361 \rangle$  and  $\{114\} \langle 481 \rangle$ , and were normally recrystallized from cold-rolled steel, while the  $\alpha^*$ -fiber recrystallization texture observed in this study was obtained from warm-rolled steel. It is also noted that if the rolling direction is changed between the two stages (Routes B and C), the extension of the  $\alpha^*$ -fiber to the  $\gamma$ -fiber ( $\{111\} \langle 231 \rangle$ ) can be eliminated.

### The influence of warm cross-rolling route on grains size

It has been noted in Fig. 7e that if the rolling direction is swapped between the two warm rolling stages (Routes B and D), the average grain areas after annealing can be considerably reduced by 30–50% as compared to those rolled in the same direction in the two stages (Routes A and C). The decrease in the recrystallized grain size by cross rolling may be attributed to shear band formation in the second warm rolling process. Huh et al. [56] have shown that, although cross-rolling does not affect the total dislocation density in the specimen, the dislocation configuration with respect to the new reference frame of cross rolling has changed, which leads to a microstructurally hardened dislocation structure. As a result, slip tends to be considerably impeded in cross-rolled specimens and an additional deformation mechanism, e.g., shear banding, is needed to

accomplish further deformation. The formation of shear bands in the microstructure provides more potential nucleation sites for the subsequent recrystallization; thus, the specimens after cross rolling show smaller grain sizes than those after conventional rolling.

### The influence of warm-rolling route on magnetic properties

The magnetic properties of electrical steels, e.g., the magnetic flux density, permeability, saturation magnetization, and core loss, are affected by a number of material factors, including the silicon content, sheet thickness, grain size, texture, etc. The high silicon content (6.5 wt%) in the steel of this research considerably reduces the saturation magnetization since the substituting silicon atoms reduces the number of ferromagnetic iron atoms in the lattice [55]. This also reduces the magnetocrystalline anisotropy [56] and magnetostriction [55].

Some researchers [57] showed that grain size played an important role in the magnetic flux density of electrical steel, i.e., the magnetic flux density tended to decrease with increasing grain size if the magnetization field strength was greater than  $\sim 300$  A/m. Others, e.g., Lee et al. [58], revealed that the magnetic flux density was only slightly affected by grain size (i.e.,  $< 1\%$ ), while the magnetocrystalline anisotropy (due to crystallographic texture) had a close correlation with the magnetic flux density. The magnetocrystalline anisotropy energy (MAE) can be calculated from the measured texture, i.e.,  $MAE = K_1(h_1^2h_2^2 + h_2^2h_3^2 + h_3^2h_1^2)$  (neglecting the isotropic and higher order terms), where  $h_1, h_2, h_3$  are the direction cosines of the magnetization direction in the crystal coordinate system ( $[100]$ - $[010]$ - $[001]$ ), and  $K_1$  is the first-order magnetocrystalline anisotropy constant. In this study,  $K_1$  for the 6.5 wt% silicon steel is calculated as  $2.132 \times 10^4 \text{ Jm}^{-3}$  using the linear relationship between  $K_1$  and the silicon content as reported by Tarasov [56].

The MAE in the rolling and transverse directions of the samples processed by the four warm rolling routes (after final annealing) are compared in Figs. 11a, b, respectively, to the measured magnetic flux densities. It is seen that the MAE shows small to moderate variations among the four routes, i.e., with relative standard deviations of 3.1% and 13.5% in the

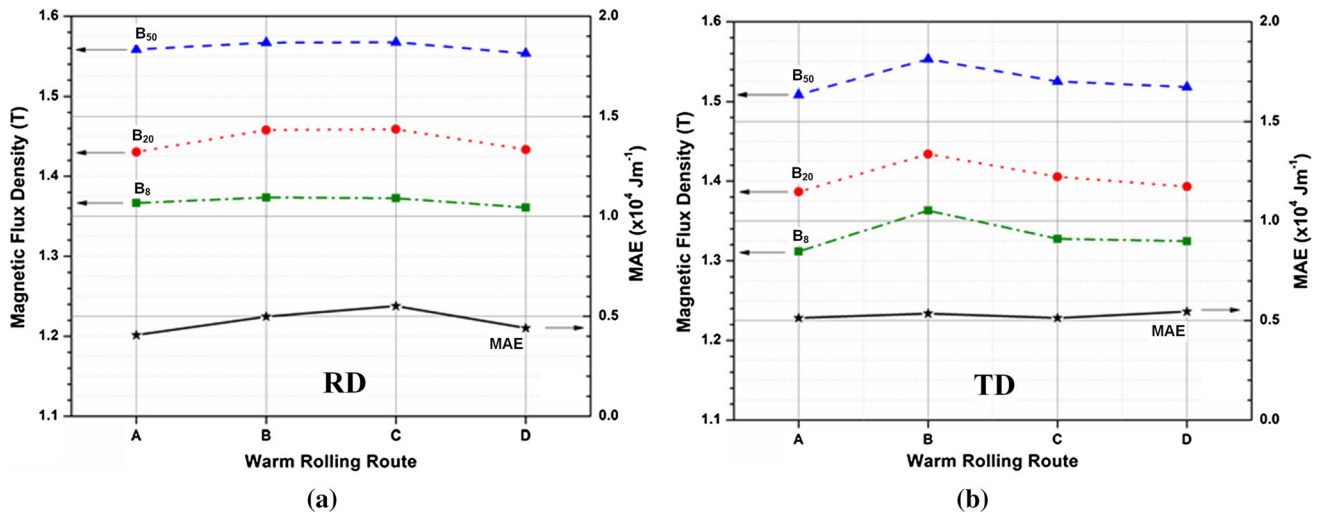


**Figure 11** Magnetic flux density vs. magnetocrystalline anisotropy energy (MAE) for different warm rolling routes: **a** in the rolling direction, **b** in the transverse direction.

TD and RD, respectively. Although the relative standard deviation of the MAE in the rolling direction is moderate (13.5%), the variation of the magnetic flux density in this direction is very small (relative standard deviation of 0.4–1.0%). On the other hand, the relative standard deviation of the MAE in the transverse direction is small (3.1%), but the relative standard deviation of the magnetic flux density in this direction is slightly larger, i.e., 1.25–1.66%. Thus, for the 6.5 wt% Si steel in this research, it is difficult to find a close relationship between the magnetic flux density and the MAE. The reason is that the change in the texture through different warm rolling routes also changed the microstructure, e.g., the grain size, which might also affect the magnetic flux density. In fact, the relatively small grain size of Route B might have contributed to the relatively large average magnetic flux density among all the routes, because a large grain size decreases the magnetic flux density when the magnetization field is greater than  $\sim 300 \text{ A/m}$  [57].

It is generally accepted that the core loss is affected by a number of material factors (texture, grains size, resistivity, thickness, etc.) and is strongly dependent on the frequency. Apparently, the small to moderate variations in the MAE shown in Fig. 11 cannot explain the core loss results illustrated in Fig. 9b, especially the large differences at high frequencies. It has been shown in the literature [59–61] that the core loss is more dependent on the grain size than on the texture. At high frequencies, the core loss is

dominated by the eddy current loss, which increases with the grain size [59, 62, 63]. Thus, the core loss at 1000 Hz shows a similar trend to the grain size after annealing (Fig. 7e), i.e., the largest grain size of Sample C might have led to the largest core loss. At lower frequencies (50 and 400 Hz), neither the MAE nor the grain size matches the trend of core losses, thus a combined effect of both the crystallographic texture and grain size might have resulted in the observed trend in core losses.

## Conclusions

Four warm rolling routes including conventional and cross rolling were utilized to process an Fe-6.5 wt% Si electrical steel at elevated temperatures (650 °C and 450 °C). The effect of warm rolling route on the microstructure, texture, and magnetic properties were investigated. The main findings can be summarized as follows:

1. Swapping the rolling direction between HRD and HTD during the two-stage warm rolling process changed the initial textures (crystal orientations), the dislocation configurations, and the active slip systems, which led to significantly different deformed microstructures and textures as compared to conventional rolling.
2. Conventional warm rolling at 650 °C resulted in cross-slip, as evidenced by numerous net-shaped slip bands in the microstructure, as well as the



activation of additional slip systems (e.g., the {112} slip), which is believed to have led to the sharpening of the rotated cube texture and the weakening of the {111} < 110 > and {112} < 110 > components.

3. Warm cross rolling at the same temperature (650 °C) enormously strengthened the rotated cube texture, which was caused by the rotation of the < 110 > //TD components (rotated from the  $\alpha$ -fiber before rolling) to the rotated cube during rolling, and by the sharpening of the initial {001} < 110 > texture due to the {112} slip.
4. During the second-stage warm rolling (450 °C), the action of the {112} slip is low; thus, conventional rolling (Route A) resulted in the weakening of the rotated cube due to the rotation of this orientation to other orientations through fragmentation and the formation of deformation bands. The change in the rolling direction from HRD to HTD (Route B) enormously enhanced the rotated cube texture, due to the rotation of the unstable initial < 110 > //TD texture (rotated from the  $\alpha$ -fiber) to the rotated cube during rolling.
5. The very strong initial {001} < 110 > texture obtained from the first-stage cross rolling was significantly weakened no matter what the rolling direction in the second stage was, i.e., HTD (Route C) or HRD (Route D), due to the rotation of this orientation to other orientations during further rolling.
6. After annealing, the textures were significantly randomized. The high silicon in the steel significantly reduced the magnetic anisotropy of the material. The magnetic flux density showed little relation with respect to the magnetocrystalline anisotropy energy.
7. The core losses of the samples processed by different warm rolling routes did not show a correlation to the magnetocrystalline anisotropy energy either, due to the complicated effect of multiple material parameters such as texture, grain size, resistivity, thickness, etc. At high frequencies (1000 Hz), the grain size appeared to have a more profound effect than the texture.

## Acknowledgements

This work was financially supported by the National Natural Science Foundation of China (Nos.51674080, 51974085) and National Key R&D Program of China (2017YFB0304105). Y. H. acknowledges the financial support from Natural Resources Canada through the Program of Energy Research and Development. H.J.X. is grateful to the support from Chinese Scholarship Council (No. 201806080099). The authors are grateful to Jian Li and Renata Zavadil for assistance in EBSD characterization.

## Compliance with ethical standards

**Conflict of interest** All authors listed have declared that they have no conflict of interest.

## References

- [1] Takashima M, Komatsubara M, Morito N (1997) {001} < 110 > texture development by two-stage cold rolling method in non-oriented electrical steel. *ISIJ Int* 37(12):1263–1268
- [2] Jiao H, Xu Y, Xiong W, Zhang Y, Cao G, Li C, Niu J, Misra RDK (2017) High-permeability and thin-gauge non-oriented electrical steel through twin-roll strip casting. *Mater Des* 136:23–33
- [3] Fang F, Zhang Y, Lu X, Wang Y, Cao G, Yuan G, Xu Y, Wang G, Misra RDK (2016) Inhibitor induced secondary recrystallization in thin-gauge grain oriented silicon steel with high permeability. *Mater Des* 105:398–403
- [4] He Y, Hilinski EJ (2017) Skew rolling and its effect on the deformation textures of non-oriented electrical steels. *J Mater Process Technol* 242:182–195
- [5] Lu X, Fang F, Zhang Y, Wang Y, Yuan G, Xu Y, Cao G, Misra R, Wang G (2017) Evolution of microstructure and texture in grain-oriented 6.5% Si steel processed by strip-casting. *Mater Charact* 126:125–134
- [6] Li HZ, Liu HT, Liu ZY, Lu HH, Song HY, Wang GD (2014) Characterization of microstructure, texture and magnetic properties in twin-roll casting high silicon non-oriented electrical steel. *Mater Charact* 88:1–6
- [7] Yao Y, Sha Y, Liu J, Zhang F, Zuo L (2016) Texture and microstructure for magnetic properties of two-stage cold-rolled Fe-6.5 wt pct Si thin sheets. *Metall Mater Trans A* 47(12):5771–5776
- [8] Liang YF, Ye F, Lin JP, Wang YL, Chen GL (2010) Effect of annealing temperature on magnetic properties of cold rolled

- high silicon steel thin sheet. *J Alloy Compd* 491(1–2):268–270
- [9] Stojakovic D, Doherty RD, Kalidindi SR, Landgraf FJG (2008) Thermomechanical processing for recovery of desired 001 fiber texture in electric motor steels. *Metall Mater Trans A* 39(7):1738
- [10] Wang J, Yang P, Zhang L, Mao W (2016) Formation of a sharp  $\{100\}$  texture in Fe-3% Si-1.7% Mn-0.05% C silicon steel sheets. *J Mater Sci* 51(22):10116–10126
- [11] Sanjari M, He Y, Hilinski EJ, Yue S, Kestens LA (2017) Texture evolution during skew cold rolling and annealing of a non-oriented electrical steel containing 0.9 wt% silicon. *J Mater Sci* 52(6):3281–3300
- [12] Kestens L, Jacobs S (2008) Texture control during the manufacturing of nonoriented electrical steels. *Texture Stress Microstruct* 2008(10):173083
- [13] Verbeken K, Kestens L, Jonas J (2003) Microtextural study of orientation change during nucleation and growth in a cold rolled ULC steel. *Scripta Mater* 48(10):1457–1462
- [14] Vanderschueren D, Kestens L, Van Houtte P, Aernoudt E, Dilewijns J, Meers U (1991) The effect of cross rolling on texture and magnetic properties of non oriented electrical steels. *Texture Stress Microstruct* 14:921–926
- [15] Yan M, Fu Y (2011) Influence of rolling direction on the texture evolution of Fe-3% Si alloy. *Acta Metall Sin* 47(1):25–33
- [16] Ushigami Y, Suga Y, Nakayama T, Takahashi N (1991) Process for production of double-oriented electrical steel sheet having high flux density. US Patent # US4,997,493A
- [17] Sonboli A, Toroghinejad MR, Edris H, Szpunar JA (2015) Effect of deformation route and intermediate annealing on magnetic anisotropy and magnetic properties of a 1 wt% Si non-oriented electrical steel. *J Magn Magn Mater* 385:331–338
- [18] Hölscher M, Raabe D, Lücke K (1991) Rolling and recrystallization textures of bcc steels. *Steel Res Int* 62(12):567–575
- [19] Maurice C, Driver J (1997) Hot rolling textures of fcc metals—Part I. Experimental results on Al single and polycrystals. *Acta Mater* 45(11):4627–4638
- [20] Paul H, Driver J, Maurice C, Piątkowski A (2007) The role of shear banding on deformation texture in low stacking fault energy metals as characterized on model Ag crystals. *Acta Mater* 55(2):575–588
- [21] Paolinelli SdC, da Cunha MA, Cota AB (2008) The influence of shear bands on final structure and magnetic properties of 3% Si non-oriented silicon steel. *J Magn Magn Mater* 320(20):e641–e644
- [22] Nguyen-Minh T, Sidor JJ, Petrov RH, Kestens LAI (2012) Occurrence of shear bands in rotated Goss ( $\{110\}$ ) orientations of metals with bcc crystal structure. *Scripta Mater* 67(12):935–938
- [23] Xu HJ, Xu YB, Jiao HT, Cheng SF, Misra RDK, Li JP (2018) Influence of grain size and texture prior to warm rolling on microstructure, texture and magnetic properties of Fe-6.5 wt% Si steel. *J Magn Magn Mater* 453:236–245
- [24] Li HZ, Liu HT, Liu Y, Liu ZY, Cao GM, Luo ZH, Zhang FQ, Lyu L, Wang GD (2014) Effects of warm temper rolling on microstructure, texture and magnetic properties of strip-casting 6.5 wt% Si electrical steel. *J Magn Magn Mater* 370:6–12
- [25] Raabe D (1995) Simulation of rolling textures of bcc metals considering grain interactions and crystallographic slip on  $\{110\}$ ,  $\{112\}$  and  $\{123\}$  planes. *Mater Sci Eng, A* 197(1):31–37
- [26] Tarasov L (1939) Ferromagnetic anisotropy of iron and iron-rich silicon alloys. *Phys Rev* 56(12):1231
- [27] Takajo S, Tomé CN, Vogel SC, Beyerlein IJ (2018) Texture simulation of a severely cold rolled low carbon steel using polycrystal modeling. *Int J Plast* 109:137–152
- [28] Xie J, Fu H, Zhang Z, Jiang Y (2012) Deformation twinning feature and its effects on significant enhancement of tensile ductility in columnar-grained Fe–6.5wt.%Si alloy at intermediate temperatures. *Intermetallics* 23:20–26
- [29] Dillamore IL, Roberts WT (1964) Rolling textures in f.c.c. and b.c.c. metals. *Acta Metall* 12(3):281–293
- [30] Plastic Deformation Structures, S. L. Semiatin, Editor, ASM Handbook, Volume 14A, Metalworking: Bulk Forming, Materials Park, Ohio, USA, 539–551. Adapted from W. F. Hosford, J. J. Jonas, W. C. Leslie, Plastic Deformation Structures, Metallography and Microstructures, Vol. 9, Metals Handbook, 9th ed. American Society for Metals, 1985, 684–691.
- [31] Dillamore I, Roberts J, Bush A (1979) Occurrence of shear bands in heavily rolled cubic metals. *Metal Science* 13(2):73–77
- [32] Hutchinson WB (2007) Deformation substructures and recrystallisation. *Mater Sci Forum* 558:13–22
- [33] Jia N, Eisenlohr P, Roters F, Raabe D, Zhao X (2012) Orientation dependence of shear banding in face-centered-cubic single crystals. *Acta Mater* 60(8):3415–3434
- [34] Wagner P, Engler O, Lücke K (1995) Formation of Cu-type shear bands and their influence on deformation and texture of rolled fcc  $\{112\}$  single crystals. *Acta Metall Mater* 43(10):3799–3812
- [35] Dorner D, Zaefferer S, Lahn L, Raabe D (2006) Overview of microstructure and microtexture development in grain-oriented silicon steel. *J Magn Magn Mater* 304(2):183–186

- [36] M.R. Barnett, Influence of warm rolling temperature on ferrite recrystallization in low C and IF steels, PhD Thesis, McGill University (1996).
- [37] Raphanel J, Van Houtte P (1985) Simulation of the rolling textures of bcc metals by means of the relaxed taylor theory. *Acta Metall* 33(8):1481–1488
- [38] Senuma T, Yada H, Shimizu R, Harase J (1990) Textures of low carbon and titanium bearing extra low carbon steel sheets hot rolled below their AR3 temperatures. *Acta Metall Mater* 38(12):2673–2681
- [39] Dillamore I, Roberts W (1965) Preferred orientation in wrought and annealed metals. *Metall Rev* 10(1):271–380
- [40] Toth L, Jonas J, Daniel D, Ray R (1990) Development of ferrite rolling textures in low-and extra low-carbon steels. *Metall Mater Trans A* 21(11):2985–3000
- [41] Ray R, Jonas JJ, Hook R (1994) Cold rolling and annealing textures in low carbon and extra low carbon steels. *Int Mater Rev* 39(4):129–172
- [42] He Y, Hilinski E, Li J (2015) Texture evolution of a non-oriented electrical steel cold rolled at directions different from the hot rolling direction. *Metall Mater Trans A* 46(11):5350–5365
- [43] Kawamata R, Kubota T, Yamada K (1997) The effect of cold rolling parameters on the recrystallization texture of non-oriented electrical steel. *J Mater Eng Perform* 6(6):701–709
- [44] Dillamore IL, Roberts WT (1964) Crystallographic texture variations through rolled aluminium and copper sheet. *J Inst Metal* 92:193–199
- [45] Inagaki H, Suda T (1972) The development of rolling textures in low-carbon steels. *Texture Stress Microstruct* 1(2):129–140
- [46] Dorner D, Zaefferer S, Raabe D (2007) Retention of the Goss orientation between microbands during cold rolling of an Fe3% Si single crystal. *Acta Mater* 55(7):2519–2530
- [47] Weinberger CR, Boyce BL, Battaile CC (2013) Slip planes in bcc transition metals. *Int Mater Rev* 58(5):296–314
- [48] Lücke K, Hölscher M (1991) Rolling and recrystallization textures of BCC steels. *Texture Stress Microstruct* 14:585–596
- [49] Hansen N, Juul J, Liu YL, Ralph B (1995) Microstructural and crystallographic aspects of recrystallization (No. NEI-DK-2144). Risoe National Lab, Roskilde
- [50] Hughes D, Hansen N (1991) Microstructural evolution in nickel during rolling and torsion. *Mater Sci Technol* 7(6):544–553
- [51] Mehdi M, He Y, Hilinski EJ, Kestens LAI, Edrissy A (2020) The evolution of cube ( $\{001\}$ ) texture in non-oriented electrical steel. *Acta Mater* 185:540–554
- [52] Park JT, Szpunar JA (2003) Evolution of recrystallization texture in nonoriented electrical steels. *Acta Mater* 51(11):3037–3051
- [53] Gobernado P, Petrov RH, Kestens LAI (2012) Recrystallized  $\{311\}$  orientation in ferrite steels. *Scripta Mater* 66(9):623–626
- [54] Homma H, Nakamura S, Yoshinaga N (2004) On  $\{h, 1, 1\}$ , the recrystallisation texture of heavily cold rolled BCC steel. *Mater Sci Forum Trans Tech Publ* 467:269–274
- [55] Quadir M, Duggan B (2004) Deformation banding and recrystallization of  $\alpha$  fibre components in heavily rolled IF steel. *Acta Mater* 52(13):4011–4021
- [56] Huh M, Engler O, Raabe D (1995) On the influence of cross-rolling on shear band formation and texture evolution in low carbon steel sheets. *Texture Stress Microstruct* 24(4):225–237
- [57] Shiozaki M, Kurosaki Y (1989) The effects of grain size on the magnetic properties of nonoriented electrical steel sheets. *J Mater Eng* 11(1):37–43
- [58] Lee K, Park S, Huh MY, Kim J, Engler O (2014) Effect of texture and grain size on magnetic flux density and core loss in non-oriented electrical steel containing 3.15% Si. *J Magn Magn Mater* 354:324–332
- [59] Qin J, Yang P, Mao W, Ye F (2015) Effect of texture and grain size on the magnetic flux density and core loss of cold-rolled high silicon steel sheets. *J Magn Magn Mater* 393:537–543
- [60] Chaudhury A, Khatirkar R, Viswanathan N, Singal V, Ingle A, Joshi S, Samajdar I (2007) Low silicon non-grain-oriented electrical steel: linking magnetic properties with metallurgical factors. *J Magn Magn Mater* 313(1):21–28
- [61] Hou CK (1996) Effect of silicon on the loss separation and permeability of laminated steels. *J Magn Magn Mater* 162(2–3):280–290
- [62] Bertotti G, Di Schino G, Milone AF, Fiorillo F (1985) On the effect of grain size on magnetic losses of 3% non-oriented SiFe. *Le J de Phys Colloq* 46(C6):385–388
- [63] Leuning N, Steentjes S, Hameyer K (2019) Effect of grain size and magnetic texture on iron-loss components in NO electrical steel at different frequencies. *J Magn Magn Mater* 469:373–382

**Publisher's Note** Springer Nature remains neutral with regard to jurisdictional claims in published maps and institutional affiliations.